APPLIED SCIENCES AND ENGINEERING

Diving beetle–like miniaturized plungers with reversible, rapid biofluid capturing for machine learning–based care of skin disease

Sangyul Baik[1†], Jihyun Lee[1†], Eun Je Jeon[2,3†], Bo-yong Park[4], Da Wan Kim[1], Jin Ho Song[1,5], Heon Joon Lee[1], Seung Yeop Han[2,3], Seung-Woo Cho[2,6,7]*, Changhyun Pang[1,8]*

Recent advances in bioinspired nano/microstructures have received attention as promising approaches with which to implement smart skin-interfacial devices for personalized health care. In situ skin diagnosis requires adaptable skin adherence and rapid capture of clinical biofluids. Here, we report a simple, all-in-one device consisting of microplungers and hydrogels that can rapidly capture biofluids and conformally attach to skin for stable, real-time monitoring of health. Inspired by the male diving beetle, the microplungers achieve repeatable, enhanced, and multidirectional adhesion to human skin in dry/wet environments, revealing the role of the cavities in these architectures. The hydrogels within the microplungers instantaneously absorb liquids from the epidermis for enhanced adhesiveness and reversibly change color for visual indication of skin pH levels. To realize advanced biomedical technologies for the diagnosis and treatment of skin, our suction-mediated device is integrated with a machine learning framework for accurate and automated colorimetric analysis of pH levels.

INTRODUCTION

Beyond mimicking the multiscale surface morphologies of various organisms, much effort has been devoted to integrating biologically inspired nanoarchitectures into smart devices and systems, spurring advances in intelligent ultraconformal bioelectronics (*1*–*3*), nano/microstructured machines and robotics (*4*, *5*), opto-electronic sensors/displays (*6*, *7*), and self-healable multimodal stretchable E-skins (*8*, *9*). Bioelectronic systems with bioinspired adhesive architectures have drawn extensive attention related to the development of effective human-machine interactions by attachment to the inner/outer surfaces of the human body (*10*, *11*). To realize advanced bioelectronics for diagnostics and therapeutics, skin-interfacial platforms require robust, adaptive adherence to skin, as well the ability to capture various biofluids (e.g., sweat, saliva, tears, and blood) for quantitative, spatiotemporal measurements of physiological information (*12*–*15*). Using techniques such as microfluidic networks (*16*, *17*), iontophoresis (*18*), and electro-osmotic flow (*19*), in situ on-body electronic systems collect sweat from the skin to provide detailed profiling of biological signals.

Thus far, notable advances in skin-interfacial systems have been presented with sweat-collective microfluidic circuits to enable analysis by passive or active detection components (e.g., lactate, creatinine, glucose, Na^+, Cl^-, pH, uric acid, or tyrosine) assembled on soft, skin-attachable patches (*16*, *20*). In particular, the pH of the human skin surface plays a crucial importance as a clinical criterion in terms of biochemical and medical studies, controlling the barrier function of skin to prevent microbial (or bacterial) colonization (e.g., by *Staphylococcus aureus* and *Malassezia*) (*21*). For inappropriate pH levels induced by exposure to dusts or sunlight, excessive hormones, or wearing protective gear, certain pH-dependent enzymes (β-glucocerebrosidase and acidic sphingomyelinase) are unable to function to form a protective membrane on human skin, often leading to the occurrence of severe skin diseases in the human body, such as inflammatory skin diseases (e.g., irritant contact dermatitis, atopic dermatitis, or acne) (*22*), infections (e.g., fungal infections or candidal intertrigo) (*23*), or skin carcinoma (*24*). For accurate in situ diagnosis and personalized treatment of skin diseases, facile and direct collection of biofluids is critically needed, along with reusable and instantaneous quantification of pH levels (*17*). Such features of pH-monitoring skin patch devices may provide a simple, cost-effective, and reliable feedback of the user's health without sophisticated systems, excessive sweating via dynamic movements (e.g., running, cycling, or swimming), or other external stimuli (e.g., electric fields or heating).

In addition, to achieve higher functionality of such smart skin patch systems, new approaches for reversibility, human-friendly use, and robust attachability are demanded. The irreversible long-term adhesion of acrylic-based adhesives might result in discomfort on engaged skin because of low air permeability (*25*, *26*). For years, to address these issues, researchers have investigated the mushroom-shaped adhesive appendages of animals (e.g., beetles or geckos), which have been influential for diverse adhesive technologies, including a highly biocompatible skin-attachable component of diagnostic wearable devices (*27*–*29*). Despite capabilities in robust and reversible adherence based on van der Waals interactions to specific surfaces, such performances are limited to dry environments. Consequently, nano/microsuckers inspired by aquatic creatures [e.g., octopus (*30*–*34*), frog (*35*, *36*), or clingfish (*37*)] have been recently developed for

[1]School of Chemical Engineering, Sungkyunkwan University (SKKU), 2066 Seobu-ro, Jangan-gu, Suwon 16419, Republic of Korea. [2]Department of Biotechnology, Yonsei University, 50 Yonsei-ro, Seoul 03722, Republic of Korea. [3]Department of Biomaterials Science and Engineering, Yonsei University, 50 Yonsei-ro, Seoul 03722, Republic of Korea. [4]McConnell Brain Imaging Centre, Montreal Neurological Institute and Hospital, McGill University, Montreal, Quebec H3A 2B4, Canada. [5]SKKU Advanced Institute of Nanotechnology, Sungkyunkwan University (SKKU), 2066 Seobu-ro, Jangan-gu, Suwon 16419, Republic of Korea. [6]Center for NanoMedicine, Institute for Basic Science (IBS), 50 Yonsei-ro, Seoul 03722, Republic of Korea. [7]Graduate Program of NanoBiomedical Engineering (NanoBME), Advanced Science Institute, Yonsei University, 50 Yonsei-ro, Seoul 03722, Republic of Korea. [8]Samsung Advanced Institute for Health Science & Technology (SAIHST), Sungkyunkwan University (SKKU), 2066 Seobu-ro, Jangan-gu, Suwon 16419, Republic of Korea.
*Corresponding author. Email: seungwoocho@yonsei.ac.kr (S.-W.C.); chpang@skku.edu (C.P.)
†These authors contributed equally to this work.

highly conformal attachment on dry or wet surfaces. However, the artificial suckers have difficulty to obtain multidirectional adherence to human skin because of its intaglio structures that cannot support physical stimuli in different directions (e.g., shear and peeling). Above all, the aforementioned architectures would be suitable for integration with conformal mechano-electric sensors (*27*, *28*, *36*, *38*) rather than biofluid-capturing pH sensors because of their structural features with the absence of specific space to continuously capture fluid-based chemical biomarker. Male diving beetles (*Hydaticus pacificus*) have evolved unique structures of spatula setae with suction cup–like structures and circular, microscale cavities on their forelegs for strong attachment and positioning against wet and irregular surfaces (*39*). The material and structural mechanics of their biological systems to develop bioinspired adhesives are not yet fully understood.

In this study, we present an unprecedented design for a smart, all-in-one adhesive with soft, bioinspired plungers that can readily capture fluids from the stratum corneum of the human skin surface (i.e., skin moisture) to provide continuous analysis of skin health. Our heterogeneous bioinspired nanoarchitecture synchronously addresses three major challenges of conventional skin-interfacial devices: (i) facile capture of skin moisture, (ii) integration of colorimetric sensors and machine learning frameworks for rapid and accurate pH analysis, and (iii) highly biocompatible and reversible attachment to irregular human skin in dry/wet conditions. Inspired by the suction plungers in the setae of male diving beetles, we established highly robust, repeatable, and multidirectional adherence to human skin in dry/wet conditions. In addition, we embedded biofluid-capturing hydrogels within the cavities of the diving beetle–inspired architectures (DIAs) to enhance suction-assisted adhesion capable of encapsulating skin moisture for facile pH analysis. Integrating machine learning techniques, we develop a software application that can automatically quantify pH levels from the color indicated by the pH-responsive hydrogels. Furthermore, we could demonstrate in vivo models for reliable and effective treatment opportunities by using our intelligent device for detecting early signs of skin disorders such as acne.

RESULTS

Diving beetle–inspired reversible microplungers for smart medical applications

Figure 1A shows the spatula setae with suction cup–like structures and circular, microscale cavities located on the forelegs of male diving beetles for advantageous attachment and positioning on the rough surfaces of female elytra during precopulatory courtship (see Supplementary Theory and fig. S1 for details) (*39*). As summarized in the schematic illustrations of Fig. 1B, the wide mushroom-shaped rigid cup provides conformal sealing, while the soft circular chamber induces the suction effect. In addition, the odorant receptor in the setae of male diving beetles may bind to specific chemical signals for chemical networking under water (Fig. 1B) (*40*). Inspired by the functionalities of male diving beetles' suckers, as illustrated in Fig. 1C, we present a design for biofluid-capturing adhesives based on microplungers with biofluid-capturing hydrogels (see Materials and Methods and fig. S2 for detailed fabrications). Photographic and scanning electron microscope (SEM) images confirm the structural uniformity of the biofluid-capturing hydrogel-embedded DIAs with diameters of 500 μm and heights of 300 μm of hexagonal array with spacing ratio 1 [SR; the distance between structures (*d*) divided by the diameter (2*r*)] (Fig. 1D). By forming a suction chamber within, the diving beetle–inspired architecture proposes an interface that readily captures and continuously analyses liquids with diagnostic biomarkers (Fig. 1E). This also enhances adhesion strength and repeatability in various directions under water (Fig. 1E). We demonstrate a simple application of skincare monitoring systems by synthesizing pH-responsive hydrogels and embedding them into the microcavities of DIAs for instantaneous, reusable, and local analysis of the epidermis (Fig. 1E). Our system presents facile, real-time recognition of pH values using a software application by harnessing a machine learning–based pH quantification model with a cross-validation framework using the input data of red-green-blue (RGB) color values (Fig. 1F). Using our device, appropriate therapeutic decision-making before pathological discovery of a disease may be possible according to the computed skin pH value, and thus, effective drug delivery would be possible in the treatment of acne vulgaris.

Adhesion of the DIAs

We measured the normal adhesive strengths of the polydimethylsiloxane (PDMS)–based patches with varying architectures in dry and underwater conditions as shown in Fig. 2A: DIA, mushroom-shaped cylindrical pillar (MCP), cylindrical pillar (CP), and flat samples (see Materials and Methods and fig. S3 for detailed adhesion tests). The DIA and MCP patches displayed higher adhesive strengths than CP and flat patches in both dry (~2.81 and ~2.25 N/cm^2, respectively) and underwater (~2.75 and ~2.09 N/cm^2, respectively) conditions, owing to enhanced contact area by the wide tips to attach conformably with the substrate. The DIA patch, particularly, showed greater normal adhesion compared to the MCP patch in dry and underwater conditions due to the suction stress induced by the elastic behavior of numerous microstructures with microcavities. After optimization of the pillar geometries for adhesion strength, we modified the softness of the DIA's widened tips by applying very soft PDMS [Young's modulus (*E*) of *s*-PDMS, ~6 to 21 kPa; see fig. S4] to enhance the contact efficiency to the attached substrate for dry and underwater conditions (Fig. 2B) (*41*). From its scale effect, as shown in Fig. 2C, we optimized the size of the DIAs with 500 μm diameter to maximize suction stress by elastic deformation of the structures under relatively low preload (among diameters of 100, 250, 500, and 3000 μm under the same preload of 1.0 N/cm^2).

We carried out finite element method (FEM) simulations to understand the elastic deformation behavior of a single DIA under varying normal forces (see the Supplementary Materials for details). As shown in Fig. 2D (i), the volume of the chamber within the DIA is easily compressed by applying normal force (2 N/cm^2), because the stress is concentrated on the thin wall of the DIA pillar. After removing the applied preload, the pressure drop is induced within the suction chamber. During the detachment process, the pressure difference for the suction effect could be yielded by volume expansion of the suction chamber [Fig. 2D (ii)]. Observing the stress distribution at the cross-sectional surface of the interface between the tip of DIA and substrate, stress is concentrated more on the inner edge than on the exterior edge [Fig. 2E (i)]. Thus, the DIA patch easily undergoes volumetric change within the microcavity, while the widened tip prevents air leakage to maintain the seal (fig. S5). Meanwhile, the MCP cannot preserve sealing of its suction chamber during detachment because the stress distribution is concentrated on the exterior edge, as shown in Fig. 2E (ii). In Fig. 2F, the *s*-DIA patch (DIA patch with *s*-PDMS tips) exhibited increasing adhesion

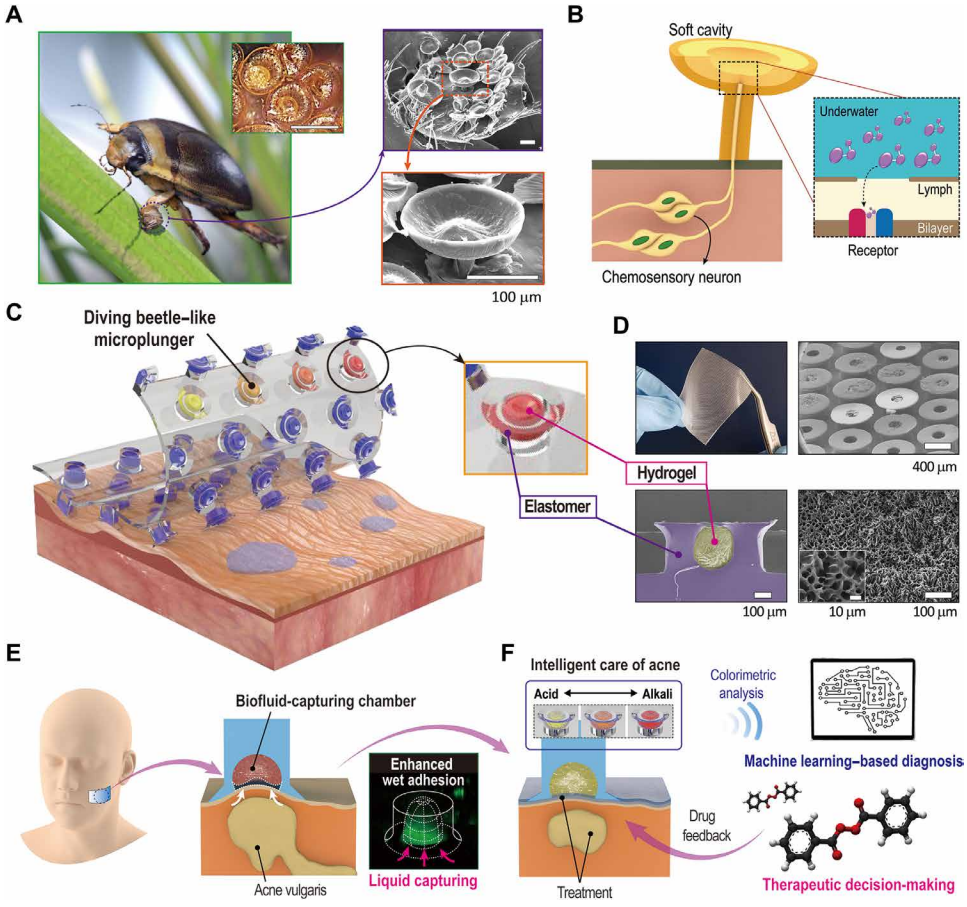

Fig. 1. The diving beetle–like reversible microplungers with biofluid-capturing hydrogel. (**A**) Photographic image of the forelegs of *H. pacificus*. SEM images magnify the spatula setae with suction cup–like structures and circular cavities. Photo credit: C. Pang, Sungkyunkwan University. (**B**) Schematic illustration of the spatula setae for suction effect and selective binding onto chemical signals to deliver as chemosensory neurons. (**C**) Schematic illustration of the adhesive patch with diving beetle–inspired suction chambers against rough and wet human skin. (**D**) Photographic and SEM images of the adhesive patch arrayed with diving beetle–inspired suction chambers. Here, the microcavities are embedded with biofluid-capturing hydrogels for rapid liquid capture. Photo credit: S. Baik, Sungkyunkwan University. (**E**) Schematic mechanism of suction chambers with embedded hydrogel for absorption of liquid and formation of vacuum chamber upon hydration for reversible attachment. (**F**) Practical applications of the adhesive patch arrayed with diving beetle–inspired suction chambers for untethered skin pH analysis for facile skincare monitoring.

strength with respect to applied preload, while the *s*-MCP and *s*-flat patch (MCP patch with *s*-PDMS tips and *s*-PDMS–coated flat patch, respectively) barely showed any increases in adhesion strengths for (i) dry and (ii) underwater conditions.

To explain the adhesive behavior of the DIAs depending on preload, we establish a simple methodological model underlying the suction effect between the microstructures and engaged surface by estimating the volumetric change of the chamber using the FEM simulation as follows (fig. S6)

$$\sigma_S = P_0(kF_p - 0.0045)\cdot\pi R^2 \cdot n \quad (1)$$

where P_0 is the initial air pressure under ambient conditions (~101.3 kPa), k is the estimated constant of volumetric change (~0.0407 $N^{-1}\cdot cm^2$), F_p is the applied preload, R is the radius of the tip of the DIA, and n is the number of DIAs per unit area (~400 cm^{-2}) (see fig. S6 and the Supplementary Materials for details). Notably, the suction stress induced solely by the volume changes can adapt equally in both dry and wet conditions, because the capillary rise of water molecules cannot occur in the microchamber due to hydrophobicity of the DIAs (fig. S7). These experimental measurements are in close agreement with our theoretical predictions (see green dotted line in Fig. 2F) for Eq. 1.

s-DIAs embedded with biofluid-capturing gels for enhanced wet adhesion and liquid capture

To maximize the capabilities of attachment under low preload for our adhesive, we designed a hybrid structure embedded with biocompatible hydrogel [polyacrylamide (PAAm)] inside the chambers of *s*-DIAs (Fig. 3A). Then, we compared the adhesive strengths of the hydrogel-embedded *s*-DIAs (H-*s*-DIAs) to the *s*-DIAs without hydrogel and the bare hydrogel patch depending on contact time with deionized water (Fig. 3B). In both dry and underwater environments, the adhesion strength of H-*s*-DIAs was saturated and maintained after 90 min of contact time, while the adhesion of the bare hydrogel patch markedly declined after 120 min of contact time. The adhesion strength of *s*-DIAs was unchanged depending on contact time. This phenomenon may simply be explained through the model of interfacial fluid mechanics on the porous polymer-substrate interface, as depicted in Fig. 3C (*42*, *43*). The rigid PDMS structure

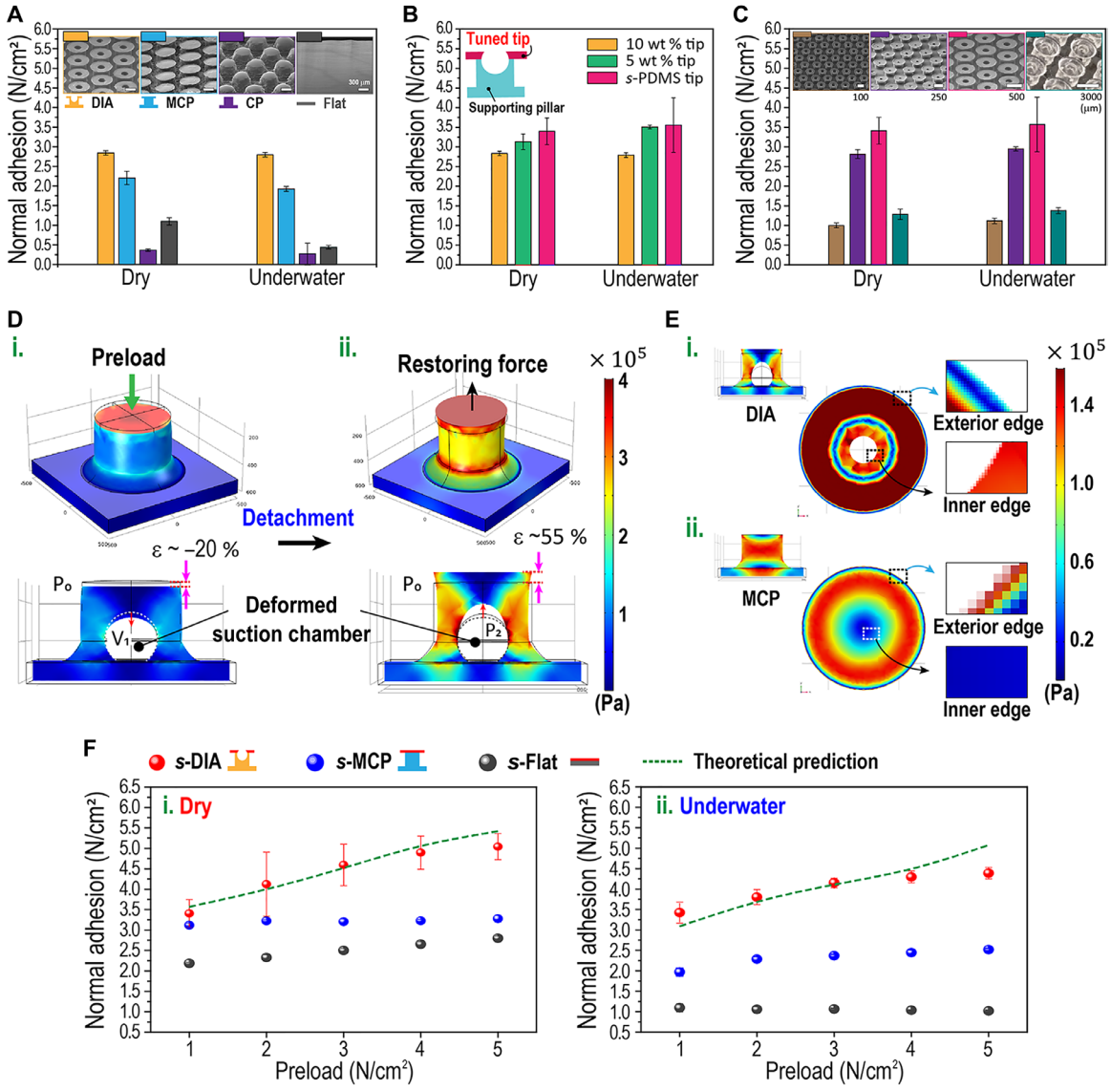

Fig. 2. Adhesion of the DIAs via structural deformation in dry and wet conditions. (**A**) Profiles of normal adhesion for different adhesive samples against silicon wafers in dry and underwater conditions. A preload of 2 N/cm^2 is applied for each measurement. (**B**) Measurements of normal adhesion in dry and underwater conditions with varied material properties of the DIA tip. wt %, weight %. (**C**) Measurements of normal adhesion in dry and underwater conditions for s-DIAs of different diameters. (**D**) (i) FEM simulation analysis of stress distribution during the application of a 2 N/cm^2 preload. (ii) Volume expansion of the inner chamber during detachment to yield the suction effect. (**E**) Comparison of stress distribution via FEM simulation for the bottom surface of (i) DIA and (ii) MCP. (**F**) Predicted (green) and experimental results of normal adhesive strength in dry and underwater conditions corresponding to preload for different adhesive samples.

with microcavity could maintain the optimized state of the swollen hydrogel for maximized underwater adhesion, as shown in Fig. 3C (ii). Hence, the hydrogel trapped within the PDMS-based pillar maintains its optimized adhesive state by asymmetrically absorbing water compared to the bare hydrogel patch, as shown in Fig. 3C. We then observed control of swelling behavior for the embedded hydrogels mixed with fluorescein isothiocyanate via confocal fluorescence microscopy and SEM (Fig. 3D). We monitored swelling of the dehydrated hydrogel [Fig. 3D (i)] upon contact with water molecules until the volume of the suction chamber increased and observed that the hydrogel retained its volume even after 2 hours [Fig. 3D (ii)]. Depending on the amount of absorbed water in the hydrogel pores, it was observed that the pore size of the hydrogel could be adjusted from nano- to microscale (radii of hydrogel pores were observed from ~200 nm to ~100 μm; fig. S8). We further measured the adhesion strength for preoptimized swollen H-*s*-DIA by applying different preloads (1 to 5 N/cm^2) in dry and underwater conditions to understand the structural effect of the embedded hydrogels inside the DIA chambers. As shown in Fig. 3E, the measurements noted that the H-DIA samples showed early saturated adhesion (maximum ~6.0 N/cm^2 for dry conditions and maximum ~5.6 N/cm^2 for underwater conditions) induced by maximized suction stress under a low preload of ~2 N/cm^2 with high repeatability (<100; see Fig. 3F). The pressure difference (ΔP) is easily maximized due to the shape of DIA with embedded hydrogel that can push out the remaining air within the chamber of DIA under a low preload of ~2 N/cm^2, forming

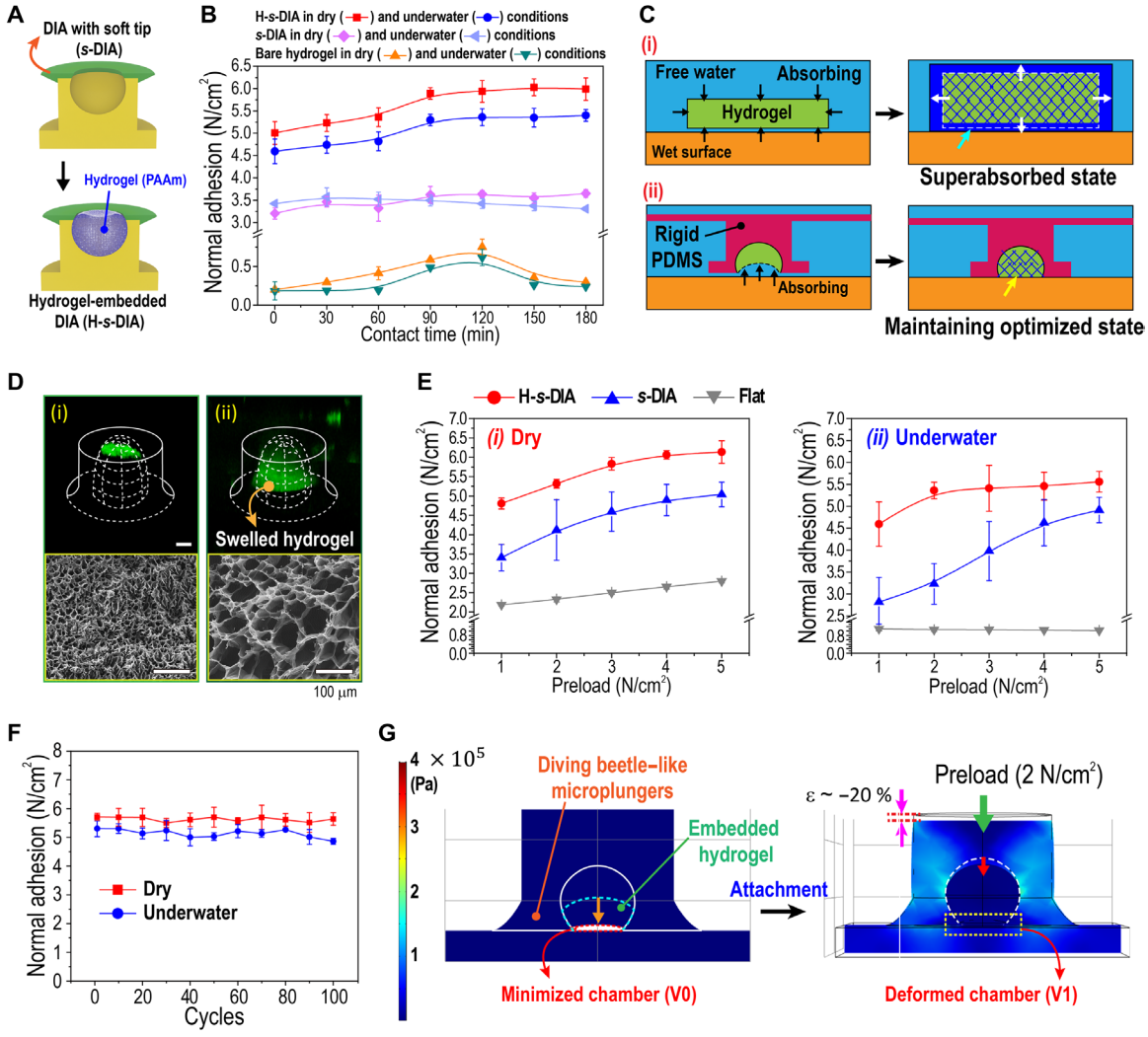

Fig. 3. Adhesive mechanism and performance of the DIAs embedded with biofluid-capturing hydrogels (H-*s*-DIAs) in dry and wet conditions. (**A**) Schematic illustration of the *s*-DIA embedded with hydrogel for instantaneous capture of liquids. (**B**) Measurements of normal adhesion for H-*s*-DIA in dry (red) and underwater (blue) conditions, *s*-DIA in dry (violet) and underwater (sky blue) conditions, and bare hydrogel in dry (orange) and underwater (green) conditions with respect to contact time. (**C**) Schematic illustration of the interfacial fluid transport on the hydrogel-substrate interface for the (i) bare hydrogel before and after liquid absorption and the (ii) H-*s*-DIA before and after hydrogel swelling within its inner chamber for the optimized state. (**D**) Confocal fluorescence microscopy images of the embedded hydrogel (i) before and (ii) after the hydrogel is swelled for 2 hours. (**E**) Adhesive performances of the H-*s*-DIA adhesives in different states with varying preloads applied in (i) dry and (ii) underwater conditions. Here, the different states of the H-*s*-DIAs consist of H-*s*-DIA before contact (orange), H-*s*-DIA after contact for 2 hours (red), H-*s*-DIA (blue), and flat samples (gray). (**F**) Cyclic measurements of normal adhesion for H-*s*-DIA after 2 hours of contact time in dry and underwater conditions. (**G**) FEM simulation analysis of the stress distribution and structural deformation of an H-*s*-DIA during the application of a 2 N/cm^2 preload. After the application of a weak preload, the volume of the suction chamber is effortlessly minimized by swelled hydrogel, inducing a vacuum-like state within the chamber.

a vacuum-like chamber (see simulation results of Fig. 3G; $\Delta P_{max} \approx P_0$, $\because VR \approx 0$). In addition, relative to the dehydrated hydrogel, the pre-swollen hydrogel is able to empty out air molecules inside the DIA chambers effortlessly (fig. S9).

To demonstrate a potential application of biofluid-capturing, human-attachable devices, we then validated attachment capabilities by measuring the adhesion of the as-prepared H-*s*-DIA patch against pigskin in various directions (see Materials and Methods and fig. S10 for detailed adhesion tests). With the aid of biofluid-capturing hydrogels, the H-*s*-DIA adhesive exhibited superior adhesive stresses in multiple directions compared to *s*-DIA samples without hydrogel (Fig. 4A). Using our well-optimized bioinspired patch device, we demonstrated that the H-*s*-DIA adhesive is capable of instantaneous biofluid capture on the epidermal layer of skin (Fig. 4B). This is mainly attributed to the aid of suction stress inside the hydrogel chamber and the liquid collection behavior at the interface between PDMS and hydrogel, explained by the directional wetting driven by the suction effect and surface energy gradient (*44*) (see Supplementary Theory and fig. S11 for details). To demonstrate the behaviors of hydrogel and water molecules during the in situ water collection process, confocal fluorescence microscopic images show capture of biofluid-like liquid into a chamber of H-*s*-DIA adhesive against a pigskin replica of rough morphology (Fig. 4B).

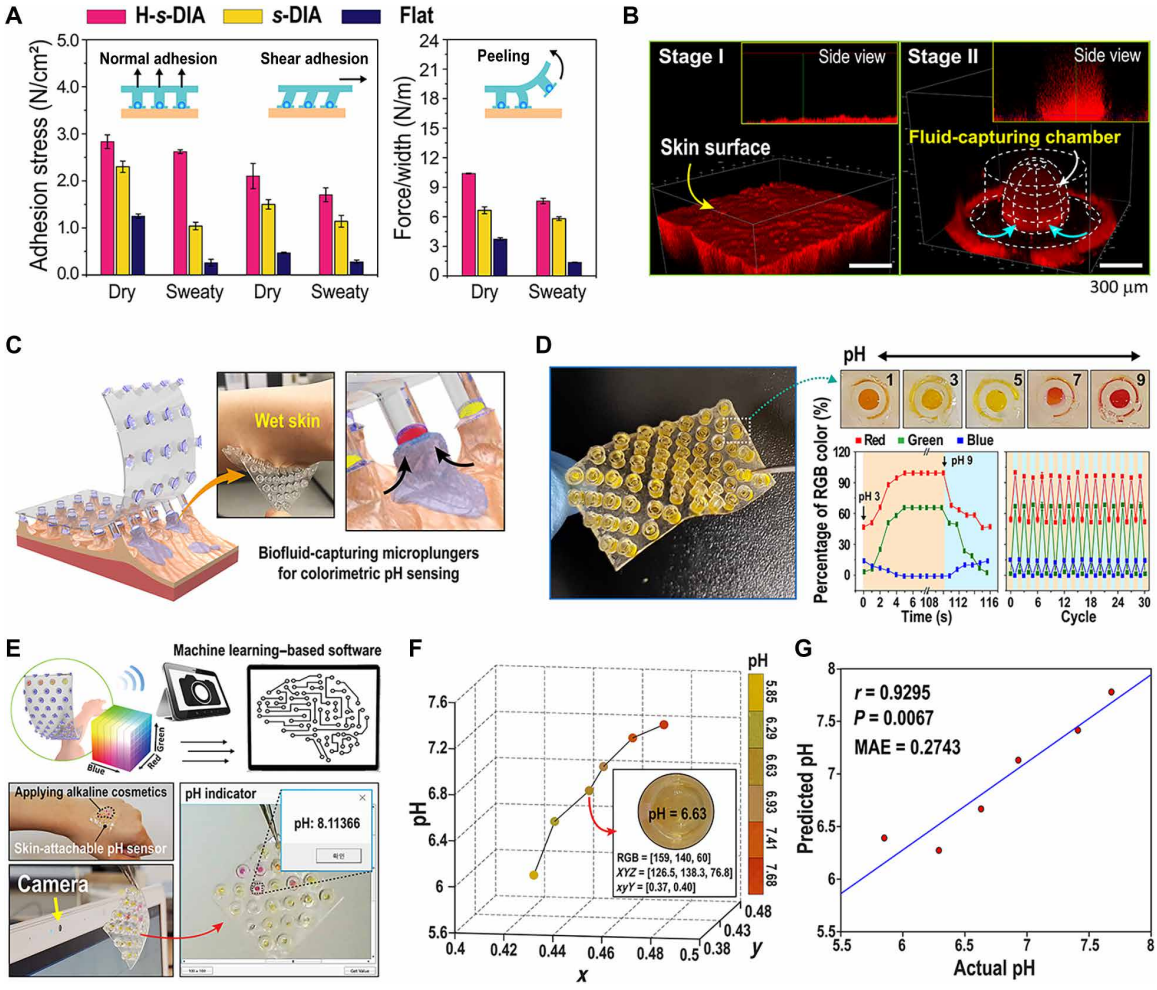

Fig. 4. Applications of the H-*s*-DIA patch on human skin for pH diagnosis and machine learning–based quantification. (**A**) Profiles of normal, shear, and peeling adhesion of H-*s*-DIA against dry and sweaty pigskin. (**B**) Confocal fluorescence microscopy of liquid capture into the embedded hydrogel chamber of H-*s*-DIA [red, mixture of fluorescent dye (rhodamine 6G), water, and silicon oil]. (**C**) Schematic illustration of the adhesive patch with skin-attachable, biofluid-capturing suction chambers. The inset shows a representative photographic image of H-*s*-DIAs of 3-mm tip diameters attached to wet human skin. Photo credit: S. Baik, Sungkyunkwan University. (**D**) Photographic image of the diving beetle–inspired adhesive embedded with colorimetric hydrogel for reversible skincare monitoring. Time-dependent profiles of red, green, and blue color percentages and cyclic measurements of red, green, and blue color percentages for different pH values of 3 and 9 on skin. (**E**) Software program for quantifying pH values via supervised machine learning. The software automatically provides pH value by converting RGB values of the captured hydrogel image into *x* and *y* values. Photo credit: S. Baik, Sungkyunkwan University. (**F**) Scatter plot of colors (i.e., *x* and *y* values) and pH values. An example image is shown with its color and pH values. (**G**) Correlation between actual and predicted pH values.

Bioinspired, biofluid-capturing patch device for intelligent pH monitoring

As a proof of this concept shown in Fig. 4C, we simply embedded pH-responsive phenol red/PAAm–based hydrogel (*45*) into the chambers of *s*-DIAs (PR/PAAm-*s*-DIA; 3 mm diameter with a width-to-depth ratio of 1) for colorimetric pH monitoring of biofluids (see movie S1 for remarkable performances of the adhesive and see the Supplementary Materials and figs. S12 and S13 for detailed synthesis and analysis of pH-responsive hydrogel). We observed peel-off behavior of our patches with various suction cup sizes on the skin of mice to demonstrate robust, conformal attachment on the curved skin surfaces (fig. S14). We ultimately decided upon the suction cup sizes with an outer diameter of 3 mm to design a patch that can easily distinguish the color change of the hydrogel even with the naked eye for practicality (see fig. S14D). As shown in Fig. 4D, our adhesive sensor for continuous, reversible pH detection using optically functionalized hydrogel exhibits fast response time (~5 s; see movie S2 for details) and reusability (>30) depending on pH changes. To establish an in situ, real-time pH value recognition by our adhesive device, we developed an in-house software application with a machine learning technique that can automatically quantify pH levels from the color indicated by the PR/PAAm-based hydrogel within the array of DIA chambers (see Fig. 4E and movie S3 for detailed measurement). Here, we used linear regression with a leave-one-out cross-validation framework (see Materials and Methods; fig. S15). Specifically, we converted RGB values into *x* and *y* values in a two-dimensional chromaticity diagram (*46*) and fed them into the linear regression to predict pH values. The *x* and *y* values showed a linearly increasing trend according to the pH values (Fig. 4F), where these color values significantly predicted pH [Pearson's correlation between

actual and predicted pH values r = 0.93; $P < 0.01$; mean absolute error (MAE) = 0.27; Fig. 4G]. These results indicate the effectiveness of our machine learning–based pH quantification system for accurate diagnosis of skin pH.

Applications of the bioinspired patch device for in situ diagnostics of acne-affected skin

For potential applications, we verified that the pH quantification model based on our intelligent H-*s*-DIA device can be valid for in vivo analysis (Fig. 5A). As calculated by the machine learning quantification with our skin-attachable colorimetric device, the pH values were consistent with the in vivo pH values measured by a commercial potentiometric pH meter (see Materials and Methods for details), showing low discrepancy (MAE = 0.14; Fig. 5B). The predicted in situ skin pH of our device could be a primary indicator of the clinical manifestation of acne. As skin pH is monitored with our simple skin-attachable device, we could have earlier diagnostic information of acne compared with conventional visual observation (pathology score monitoring); this allows reliable and preemptive drug administration through its efficient feedback without drug (e.g., antibiotics and steroids) overuse and resistance.

On the basis of preliminary analysis with our device, we establish the pathological criteria of pH value (the pH value is above 7) for therapeutic decision making of acne, which enables the designation of a proper time frame for medication administration (0 to 2 days after acne induction; see Materials and Methods and fig. S16 for details). With the aid of our intelligent patch device for pH feedback, more effective acne treatment could be achieved in advance compared with the conventional method based on pathology score monitoring (see Fig. 5, C to F). Here, skin pathology associated with acne was scored as following a previous literature (*47*) (the timing of medication administration, at which pathological score is above 4, is 3 to 5 days later in conventional treatment; see Materials and Methods and fig. S16 for details).

To demonstrate the superior efficiency of the therapeutic feedback of our straightforward pH monitoring device, we investigated four different cases: normal skin (black dots), acne lesions without treatments (gray dots), acne lesions treated with conditional drug administration upon pathology score feedback (blue dots), and pH value feedback (red dots) after acne induction in mice (Fig. 5C). The pH monitoring feedback group (red dots) received drug treatment earlier (average 3 days and maximum 4 days) than the pathology score feedback group (blue dots) (see blue arrows in Fig. 5C; drug treatment timing of each individual mouse). In accordance with the pH analysis, there was a significant difference in skin pathological status between the pathology score feedback group and the pH monitoring feedback group from the third day after acne induction (Fig. 5, E and F). In addition, the pH and skin pathological status of the pH monitoring feedback group were close to those of the normal skin group from the fifth day after the experiment began (Fig. 5, E and F). These results show a good correlation with the histological analysis (Fig. 5F; see figs. S17 and S18 for details). Hematoxylin and eosin (H&E) staining indicated skin regeneration and reduction of epidermal/follicular wall thickening in the pH monitoring feedback group (Fig. 5F). The epidermal thickness of the pH monitoring feedback group is 17.9 ± 4.2 μm, which is 27% of that of the pathology score feedback group (65.6 ± 12.5 μm). Here, this was the lowest value in all experimental groups, suggesting that skin pH can be an important indicator for acne treatment (Fig. 5F and figs. S17 and S18). Toluidine blue (TB) and Gram staining support the reduced infiltration of mast cells into the lesion site and inhibition of Gram-positive *Cutibacterium acnes* (C. acnes) growth (see purple layer in Fig. 5F; Gram-stained images) in the pH monitoring feedback group. Immunohistochemical staining of a hyper-keratinization response marker (keratin 14) and *C. acnes*–induced inflammatory response marker [matrix metalloproteinase-9 (MMP-9)] suggests that early drug treatment enables effective tissue healing by reducing the expression of MMP-9, which plays a predominant role in inflammatory matrix remodeling and hyperproliferation of acne skin (*48*). We note that our device with biofluid-capturing hydrogel has a similar therapeutic effect to 3M Tegaderm (a gold standard treatment; fig. S17), which provides the protection of the target lesion and the capability to maintain a moist environment.

DISCUSSION

We have developed an adhesive based on bioinspired microplungers for biocompatible, reversible, and resistant adhesion in various directions and instantaneous capture of skin moisture. Owing to cavities and embedded biofluid-capturing hydrogels in microplungers, our patch devices can maximize adhesion performances and the ability to capture biofluids on the skin. Through further work, our bioinspired adhesive may be integrated into biosensor modules with machine learning frameworks for efficient, noninvasive analysis and profiling of biosignals such as skin pH value. Our intelligent health care system could provide support for therapeutic decision making via pH quantification of in vivo models.

Skin pH is influenced by various endogenous factors, such as ethnicity and gender, so it is important to understand skin pH by considering these factors together and make appropriate clinical decisions. For example, individuals with darker skin usually have lower skin pH than those with lighter skin, because the amount of epidermal lipid is relatively higher in darker skin (*49*). In another example, men generally sweat more than women, so their skin surface is relatively acidic. Sweat has a pH of 5 to 6, but the evaporation of moisture makes the skin more acidic (*50*). Therefore, we believe that future investigation of skin pH across diverse ethnicities and genders would supplement our research and be able to provide users with more personalized therapy.

MATERIALS AND METHODS

Fabrication of diving beetle–inspired adhesives

We prepared perforated pillars with cavity-like suction chambers by using previously developed methods such as photolithography, partial-filling techniques, and replica molding (see the Supplementary Materials for details) (*51*). To fabricate mushroom-shaped pillars with microcavities (DIAs), the liquid precursor of the PDMS was spin-coated onto a glass substrate at 1200 rpm for 60 s. The perforated pillar patch was then selectively transferred onto the glass substrate with a thin PDMS layer. No exterior pressure was applied during the inking step for 10 s. The inked adhesive patch was placed onto a clean glass substrate with perforated pillars facing downward and cured for 2 hours at 70°C. Next, to fabricate DIAs with soft tips (*s*-DIAs), liquid precursor of the soft PDMS (*s*-PDMS), composed of 40 μl of ethoxylated polyethylenimine per 10 g of PDMS, was transferred onto the DIA tips using the same process previously performed. Here, the *s*-PDMS–inked adhesive patch was placed onto

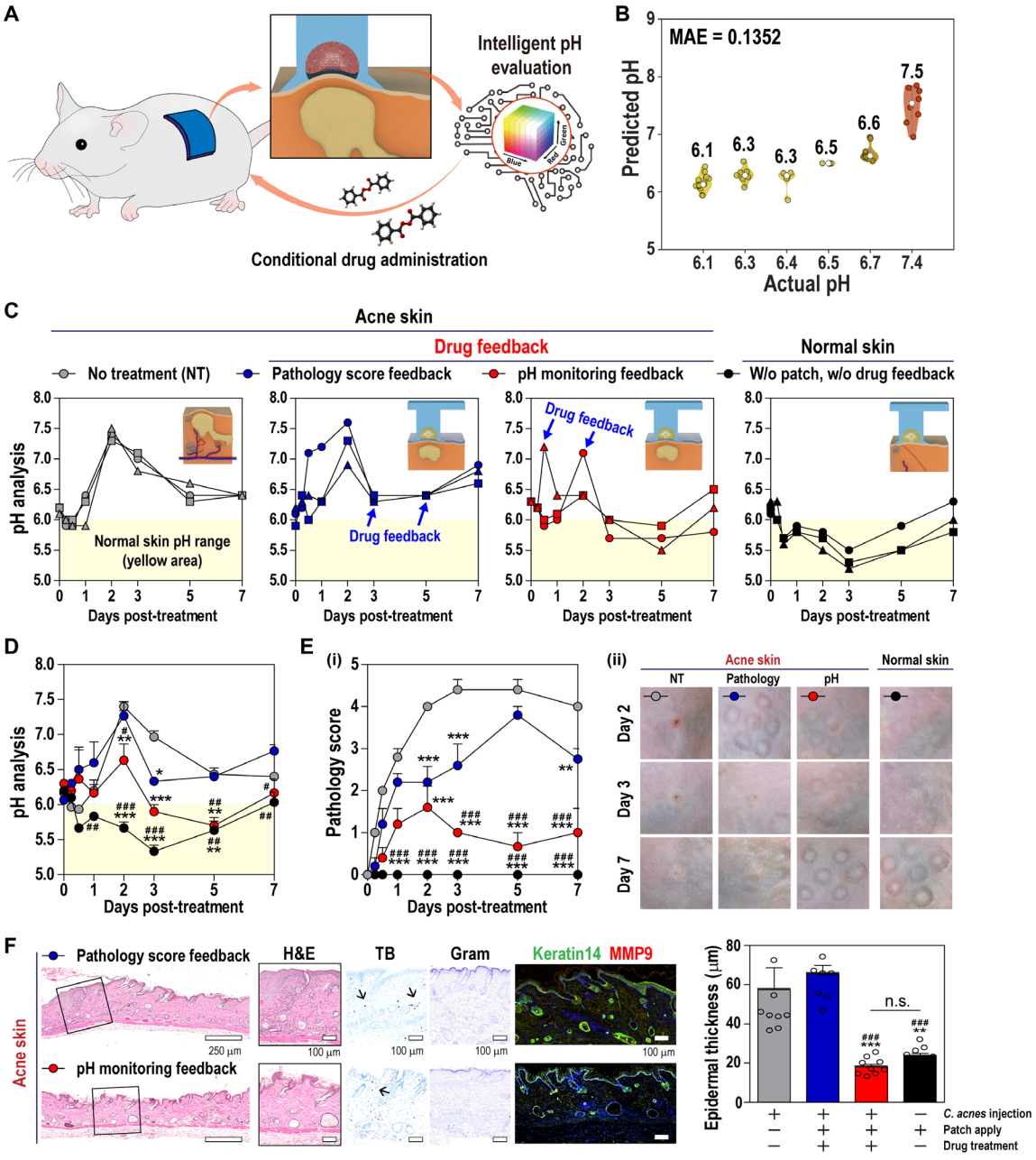

Fig. 5. Evaluating the feasibility of the H-*s*-DIA patch as a smart skincare system. (**A**) Schematic illustration of a mouse study. (**B**) Scatter plot showing actual and predicted pH values of all data. (**C** to **F**) Effect of conditional drug administration in a mouse acne model. All groups except the no treatment (NT) group were treated with patch: the NT group received no drug treatment after acne induction (gray); the pathology score feedback (pathology) group received drug treatment if the pathology score was 4 or higher (blue); the pH monitoring feedback (pH) group received drug treatment if the skin pH value was 7 or higher (red); and the normal skin group did not induce acne (black). The pH value analyses in individual mice (C) and groups (D). (E) Skin pathology score analysis (i) and representative images of acne lesions in each group (ii). (F) Histological analyses of skin tissues using H&E, TB, Gram, and immunohistochemical staining. Scale bars, 250 μm or 100 μm. Black arrows indicate TB-positive cells. Quantification of epidermal thickness using H&E-stained specimens. One-way or two-way analysis of variance (ANOVA) was used to determine statistical significance. $^{*}P < 0.05$, $^{**}P < 0.01$, and $^{***}P < 0.001$ versus NT. $^{\#}P < 0.05$, $^{\#\#}P < 0.01$, and $^{\#\#\#}P < 0.001$ versus pathology score feedback. n.s., not significant.

a clean glass substrate with DIAs facing upward and cured for 2 hours at 90°C (fig. S2A).

Preparation of PAAm hydrogel

We prepared a PAAm hydrogel by mixing the precursors. Here, the precursors consist of acrylamide (AAm), *N*,*N*′-methylene(bis) acrylamide (BAAm), *N*,*N*,*N*′,*N*′-tetramethylethylenediamine (TEMED), ammonium persulfate (APS), and water. To prepare a pre-gel solution, 1.03 g of AAm and 337 μl of BAAm (0.02 g/10 ml) as a cross-linker were mixed. We added 8.2 μl of TEMED as an accelerator and 102 μl of 0.2 M APS as an initiator. Afterward, the pre-gel solution was mixed in a beaker, and the solution was cured at 80°C for 1 hour.

To measure the porosity of PAAm-based hydrogel structures, the pore size was measured after freeze-drying the PAAm-based hydrogel swelled according to the water contact time (fig. S2B).

Fabrication of hydrogel-embedded H-*s*-DIA patches

To inject the pre-gel solution into the microcavities of the *s*-DIAs, the as-prepared patch was first treated with O_2 plasma for 1 min. The patch was then placed on a Teflon-coated substrate, and the pre-gel solution was poured on top to permeate the microhole chambers. Here, to selectively fill the pre-gel solution, we removed the residual solution between the micropillars using blotting paper. Last, the sample was cured at 80°C for 1 hour (fig. S2A). Experiments with human subjects using the H-*s*-DIA patch were performed after approval from the Institutional Review Board (IRB) was initially received for both subject and parental assent (IRB approval no. SKKU 2018-05-012), following school board policies.

Adhesion test

Details of all the adhesion measurements are provided in the Supplementary Materials.

Machine learning–based pH quantification

Leveraging supervised machine learning with cross-validation, we built an automated pH quantification model that can provide a pH value of the input image. The pH values of the input images varied from 5.85 to 7.68. We first converted the RGB values of all pixels in the input image into the *XYZ* values using the following equation

$$\begin{bmatrix} X \\ Y \\ Z \end{bmatrix} = \begin{bmatrix} 0.4125 & 0.3576 & 0.1804 \\ 0.2127 & 0.7152 & 0.0722 \\ 0.0193 & 0.1192 & 0.9503 \end{bmatrix} \begin{bmatrix} \mathrm{R} \\ \mathrm{G} \\ \mathrm{B} \end{bmatrix}$$

and then calculated *xyY* values as follows

$$x = \frac{X}{X + Y + Z}$$

$$y = \frac{Y}{X + Y + Z}$$

$$Y = Y$$

Through this conversion, we could obtain x and y values, which represent chromaticity and luminance of the color in a two-dimensional chromaticity diagram (*46*). We performed pH prediction based on leave-one-out cross-validation by separating the training and test dataset. Specifically, among seven independent datasets, six cases were assigned as the training data and the left-out case as the test data. A linear regression model was constructed using the x and y values as independent variables within the training data, and it was applied to the test data to predict its pH value. It was repeated seven times with different segments of training data. Prediction accuracy was assessed by calculating Pearson's correlation between the actual and predicted pH values as well as their MAE. The significance of the correlation was assessed via 1000 permutation tests by randomly shuffling pH values. Through this approach, a null distribution was constructed. If the real correlation coefficient did not belong to the 95% of the null distribution, it was deemed significant ($P < 0.05$). We developed an in-house software for pH detection by integrating the above procedures. Researchers who are interested can contact the corresponding author. The brief pipeline is as follows: (i) take a picture using a camera and (ii) pick the area that we want to know the pH value. Then, the software automatically provides the pH of the selected area (movie S3).

Validity of the pH quantification model

The validity of our machine learning–based pH quantification model was assessed using an independent dataset of animal models. We applied the trained model to the skin patch data to predict their pH and assessed MAE between measured and predicted pH values.

Animal studies

The animal experiments using the *C. acnes*–induced acne model were reviewed and approved by the Institutional Animal Care and Use Committee (IACUC) of the Yonsei University (approval number: IACUC-A-202002-1011-03) and the Institutional Biosafety Committee (IBC) of the Yonsei University (approval number: IBC-A-202001-227-01). To prepare the acne model, a *C. acnes* strain (KCTC 3314) was acquired from the Korean Collection for Type Cultures (KCTC; Daejeon, Korea). The acne mouse model was prepared as described in previous literature (*52*). Briefly, mice (SKH1-hr, 7-week-old male; OrientBio, Seongnam, Korea) were anesthetized with ketamine (100 mg/kg; Yuhan, Seoul, Korea) and xylazine (20 mg/kg; Bayer Korea, Ansan, Korea) and then injected intradermally with 1×10^7 colony-forming units of *C. acnes* in 25 μl of phosphate-buffered saline. After acne induction, the mice were randomly divided into experimental groups. For drug treatment, 20 μl of 5% (w/v) benzoyl peroxide (Sigma-Aldrich, St. Louis, MO, USA) was topically administered to the lesion site (*53*).

Optimization of therapeutic decision-making criteria

The results of preliminary animal experiments showed that the patch-only group and no other group exceeded pH 7 and pathology score of 4 (fig. S16C) after acne induction. In that group, a time-point gap can be noticed in that the marked increase in the pH value occurred earlier than that of the pathology score (fig. S16, B and C). Thus, we hypothesized that if we monitor pH value changes, we will be able to detect skin troubles in advance and treat them more efficiently than conventional acne management methods based on pathology score monitoring (visual observation). The minimal value of pH and pathological skin status (pathology score) for administering drug, which are 7 and 4, respectively, was decided upon lesion characteristics from a previous experiment (fig. S16).

Mouse skin pH measurement

The pH of mouse skin was measured in two ways. As a conventional method, pH was measured according to the manufacturer's manual of "Howskin" (Innoinsight Incorporated, Seoul, Korea), a skin analyzing device. When using our adhesive device, the device was first attached to the skin surface or acne lesion and removed at predetermined time points, and the pH value was computed using the changed RGB information of the biofluid-capturing hydrogel. The used patch was reused in the same mice until the end of the experiment period.

Skin pathology score assessment in mice

Skin pathology associated with acne was scored as in previous literature (*47*). Briefly, the score was determined according to the degree of the following four items: erythematous change (no = 0, mild = 1, and marked = 2), papule (flat = 0, small = 1, and large = 2), eschar

(no = 0, mild = 1, and marked = 2), and xeroderma (no = 0, mild = 1, and marked = 2).

Histological analyses

The skin specimens were harvested at the end of the experiment, fixed with 10% formalin (Sigma-Aldrich, St. Louis, MO, USA), and embedded in paraffin for sectioning (4 μm thickness). The prepared samples were stained with hematoxylin (Sigma-Aldrich) and eosin Y (Samchun Chemical, Seoul, Korea) (H&E staining), TB staining (Sigma-Aldrich), and crystal violet (Sigma-Aldrich) and Gram's iodine (Sigma-Aldrich) (Gram staining). The H&E-stained samples were used to measure epidermal thickness, and TB-stained samples were used to quantify the number of mast cells as previously reported (*54*, *55*). For immunohistochemical staining, the prepared sections were permeabilized with 0.2% (v/v) Triton X-100 (Wako, Osaka, Japan) and incubated with 4% (v/v) bovine serum albumin (Wako). Then, the samples were incubated with the following antibodies: mouse anti–keratin 14 (Abcam, Cambridge, CBE, UK), goat anti–MMP-9 (R&D Systems, Minneapolis, MN, USA), Alexa Fluor 488 goat anti-mouse immunoglobulin G (IgG; Thermo Fisher Scientific, Waltham, MA, USA), and Alexa Fluor 594 rabbit anti-goat IgG (Thermo Fisher Scientific). The samples were counterstained with 4′,6-diamidino-2-phenylindole (DAPI) (TCI America, Portland, OR, USA) and observed with a laser scanning confocal microscope (LSM 880; Zeiss, Jena, Germany) or a slide scanner (VS120-S5-W; Olympus, Tokyo, Japan).

SUPPLEMENTARY MATERIALS

Supplementary material for this article is available at http://advances.sciencemag.org/cgi/content/full/7/25/eabf5695/DC1

View/request a protocol for this paper from *Bio-protocol*.

REFERENCES AND NOTES

1. E. Song, J. Li, S. M. Won, W. Bai, J. A. Rogers, Materials for flexible bioelectronic systems as chronic neural interfaces. *Nat. Mater.* **19**, 590–603 (2020).
2. Y. J. Hong, H. Jeong, K. W. Cho, N. Lu, D.-H. Kim, Wearable and implantable devices for cardiovascular healthcare: From monitoring to therapy based on flexible and stretchable electronics. *Adv. Funct. Mater.* **29**, 1808247 (2019).
3. S. Park, G. Loke, Y. Fink, P. Anikeeva, Flexible fiber-based optoelectronics for neural interfaces. *Chem. Soc. Rev.* **48**, 1826–1852 (2019).
4. S. Li, R. Batra, D. Brown, H.-D. Chang, N. Ranganathan, C. Hoberman, D. Rus, H. Lipson, Particle robotics based on statistical mechanics of loosely coupled components. *Nature* **567**, 361–365 (2019).
5. A. Pena-Francesch, H. Jung, M. C. Demirel, M. Sitti, Biosynthetic self-healing materials for soft machines. *Nat. Mater.* **19**, 1230–1235 (2020).
6. Y. M. Song, Y. Xie, V. Malyarchuk, J. Xiao, I. Jung, K.-J. Choi, Z. Liu, H. Park, C. Lu, R.-H. Kim, R. Li, K. B. Crozier, Y. Huang, J. A. Rogers, Digital cameras with designs inspired by the arthropod eye. *Nature* **497**, 95–99 (2013).
7. M. S. Kim, G. J. Lee, C. Choi, M. S. Kim, M. Lee, S. Liu, K. W. Cho, H. M. Kim, H. Cho, M. K. Choi, N. Lu, Y. M. Song, D.-H. Kim, An aquatic-vision-inspired camera based on a monocentric lens and a silicon nanorod photodiode array. *Nat. Electron.* **3**, 546–553 (2020).
8. T. Someya, M. Amagai, Toward a new generation of smart skins. *Nat. Biotechnol.* **37**, 382–388 (2019).
9. D. Son, J. Kang, O. Vardoulis, Y. Kim, N. Matsuhisa, J. Y. Oh, J. W. F. To, J. Mun, T. Katsumata, Y. Liu, A. F. McGuire, M. Krason, F. Molina-Lopes, J. Ham, U. Kraft, Y. Lee, Y. Yun, J. B.-H. Tok, Z. Bao, An integrated self-healable electronic skin system fabricated via dynamic reconstruction of a nanostructured conducting network. *Nat. Nanotechnol.* **13**, 1057–1065 (2018).
10. S. Baik, H. J. Lee, D. W. Kim, J. W. Kim, Y. Lee, C. Pang, Bioinspired adhesive architectures: From skin patch to integrated bioelectronics. *Adv. Mater.* **31**, 1803309 (2019).
11. Y. Chen, J. Meng, Z. Gu, X. Wan, L. Jiang, S. Wang, Bioinspired multiscale wet adhesive surfaces: Structures and controlled adhesion. *Adv. Funct. Mater.* **30**, 1905287 (2020).
12. H. Yuk, C. E. Varela, C. S. Nabzdyk, X. Mao, R. F. Padera, E. T. Roche, X. Zhao, Dry double-sided tape for adhesion of wet tissues and devices. *Nature* **575**, 169–174 (2019).
13. M. Bariya, H. Y. Y. Nyein, A. Javey, Wearable sweat sensors. *Nat. Electron.* **1**, 160–171 (2018).
14. J. Choi, R. Ghaffari, L. B. Baker, J. A. Rogers, Skin-interfaced systems for sweat collection and analytics. *Sci. Adv.* **4**, eaar3921 (2018).
15. S. Xu, Y. Zhang, L. Jia, K. E. Mathewson, K.-I. Jang, J. Kim, H. Fu, X. Huang, P. Chava, R. Wang, S. Bhole, L. Wang, Y. J. Na, Y. Guan, M. Flavin, Z. Han, Y. Huang, J. A. Rogers, Soft microfluidic assemblies of sensors, circuits, and radios for the skin. *Science* **344**, 70–74 (2014).
16. A. Koh, D. Kang, Y. Xue, S. Lee, R. M. Pielak, J. Kim, T. Hwang, S. Min, A. Banks, P. Bastien, M. C. Manco, L. Wang, K. R. Ammann, K.-I. Jang, P. Won, S. Han, R. Ghaffari, U. Paik, M. J. Slepian, G. Balooch, Y. Huang, J. A. Rogers, A soft, wearable microfluidic device for the capture, storage, and colorimetric sensing of sweat. *Sci. Transl. Med.* **8**, 366ra165 (2016).
17. F. B. Myers, L. P. Lee, Innovations in optical microfluidic technologies for point-of-care diagnostics. *Lab Chip* **8**, 2015–2031 (2008).
18. S. Emaminejad, W. Gao, E. Wu, Z. A. Davies, H. Y. Y. Nyein, S. Challa, S. P. Ryan, H. M. Fahad, K. Chen, Z. Shahpar, S. Talebi, C. Milla, A. Javey, R. W. Davis, Autonomous sweat extraction and analysis applied to cystic fibrosis and glucose monitoring using a fully integrated wearable platform. *Proc. Natl. Acad. Sci. U.S.A.* **114**, 4625–4630 (2017).
19. L. Lipani, B. G. R. Dupont, F. Doungmene, F. Marken, R. M. Tyrrell, R. H. Guy, A. Ilie, Non-invasive, transdermal, path-selective and specific glucose monitoring via a graphene-based platform. *Nat. Nanotechnol.* **13**, 504–511 (2018).
20. Y. Yang, Y. Song, X. Bo, J. Min, O. S. Pak, L. Zhu, M. Wang, J. Tu, A. Kogan, H. Zhang, T. K. Hsiai, Z. Li, W. Gao, A laser-engraved wearable sensor for sensitive detection of uric acid and tyrosine in sweat. *Nat. Biotechnol.* **38**, 217–224 (2020).
21. E. Proksch, pH in nature, humans and skin. *J. Dermatol.* **45**, 1044–1052 (2018).
22. H. Jang, A. Matsuda, K. Jung, K. Karasawa, K. Matsuda, K. Oida, S. Ishizaka, G. Ahn, Y. Amagai, C. Moon, S.-H. Kim, P. D. Arkwright, K. Takamori, H. Matsuda, A. Tanaka, Skin pH is the master switch of kallikrein 5-mediated skin barrier destruction in a murine atopic dermatitis model. *J. Invest. Dermatol.* **136**, 127–135 (2016).
23. S. L. Percival, C. Emanuel, K. F. Cutting, D. W. Williams, Microbiology of the skin and the role of biofilms in infection. *Int. Wound J.* **9**, 14–32 (2012).
24. D. Zhou, K. Ota, C. Nardin, M. Feldman, A. Widman, O. Wind, A. Simon, M. Reilly, L. R. Levin, J. Buck, K. Wakamatsu, S. Ito, J. H. Zippin, Mammalian pigmentation is regulated by a distinct cAMP-dependent mechanism that controls melanosome pH. *Sci. Signal.* **11**, eaau7987 (2018).
25. J. M. Karp, R. Langer, Dry solution to a sticky problem. *Nature* **477**, 42–43 (2011).
26. B. Yu, S.-Y. Kang, A. Akthakul, N. Ramadurai, M. Pilkenton, A. Patel, A. Nashat, D. G. Anderson, F. H. Sakamoto, B. A. Gilchrest, R. R. Anderson, R. Langer, An elastic second skin. *Nat. Mater.* **15**, 911–918 (2016).
27. T. Kim, J. Park, J. Sohn, D. Cho, S. Jeon, Bioinspired, highly stretchable, and conductive dry adhesives based on 1D–2D hybrid carbon nanocomposites for all-in-one ECG electrodes. *ACS Nano* **10**, 4770–4778 (2016).
28. D.-M. Drotlef, M. Amjadi, M. Yunusa, M. Sitti, Bioinspired composite microfibers for skin adhesion and signal amplification of wearable sensors. *Adv. Mater.* **29**, 1701353 (2017).
29. B. Gao, X. Wang, T. Li, Z. Feng, C. Wang, Z. Gu, Gecko-inspired paper artificial skin for intimate skin contact and multisensing. *Adv. Mater. Technol.* **4**, 1800392 (2019).
30. S. Baik, J. Kim, H. J. Lee, T. H. Lee, C. Pang, Highly adaptable and biocompatible octopus-like adhesive patches with meniscus-controlled unfoldable 3D microtips for underwater surface and hairy skin. *Adv. Sci.* **5**, 1800100 (2018).
31. Y.-C. Chen, H. Yang, Octopus-inspired assembly of nanosucker arrays for dry/wet adhesion. *ACS Nano* **11**, 5332–5338 (2017).
32. Y. Qian, J. Nie, X. Ma, Z. Ren, J. Tian, J. Chen, H. Shen, X. Chen, Y. Li, Octopus tentacles inspired triboelectric nanogenerators for harvesting mechanical energy from highly wetted surface. *Nano Energy* **60**, 493–502 (2019).
33. J. H. Oh, S. Y. Hong, H. Park, S. W. Jin, Y. R. Jeong, S. Y. Oh, J. Yun, H. Lee, J. W. Kim, J. S. Ha, Fabrication of high-sensitivity skin-attachable temperature sensors with bioinspired microstructured adhesive. *ACS Appl. Mater. Interfaces* **10**, 7263–7270 (2018).
34. H. Lee, D.-S. Um, Y. Lee, S. Lim, H.-j. Kim, H. Ko, Octopus-inspired smart adhesive pads for transfer printing of semiconducting nanomembranes. *Adv. Mater.* **28**, 7457–7465 (2016).
35. D. W. Kim, S. Baik, H. Min, S. Chun, H. J. Lee, K. H. Kim, J. Y. Lee, C. Pang, Highly permeable skin patch with conductive hierarchical architectures inspired by amphibians and octopi for omnidirectionally enhanced wet adhesion. *Adv. Funct. Mater.* **29**, 1807614 (2019).
36. L. Zhang, H. Chen, Y. Guo, Y. Wang, Y. Jiang, D. Zhang, L. Ma, J. Luo, L. Jiang, Micro–nano hierarchical structure enhanced strong wet friction surface inspired by tree frogs. *Adv. Sci.* **7**, 2001125 (2020).
37. P. Rao, T. L. Sun, L. Chen, R. Takahashi, G. Shinohara, H. Guo, D. R. King, T. Kurokawa, J. P. Gond, Tough hydrogels with fast, strong, and reversible underwater adhesion based on a multiscale design. *Adv. Mater.* **30**, e1801884 (2018).
38. S. Chun, D. W. Kin, S. Baik, H. J. Lee, S. H. Bhang, C. Pang, Conductive and stretchable adhesive electronics with miniaturized octopus-like suckers against dry/wet skin for biosignal monitoring. *Adv. Funct. Mater.* **28**, 1805224 (2018).

39. Y. Chen, M.-C. Shih, M.-H. Wu, E.-C. Yang, K.-J. Chi, Underwater attachment using hairs: The functioning of spatula and sucker setae from male diving beetles. *J. R. Soc. Interface* **11**, 20140273 (2014).
40. L.-M. Song, X. Jiang, X.-M. Wang, J.-D. Li, F. Zhu, X.-B. Tu, Z.-H. Zhang, L.-P. Ban, Male tarsi specific odorant-binding proteins in the diving beetle *Cybister japonicus* sharp. *Sci. Rep.* **6**, 31848 (2016).
41. S. Baik, H. J. Lee, D. W. Kim, H. Min, C. Pang, Capillarity-enhanced organ-attachable adhesive with highly drainable wrinkled octopus-inspired architectures. *ACS Appl. Mater. Interfaces* **11**, 25674–25681 (2019).
42. R. Michel, L. Poirier, Q. van Poelvoorde, J. Legagneux, M. Manassero, L. Corté, Interfacial fluid transport is a key to hydrogel bioadhesion. *Proc. Natl. Acad. Sci. U.S.A.* **116**, 738–743 (2019).
43. L. Xue, A. Kovalev, A. Eichler-Volf, M. Steinhart, S. N. Gorb, Humidity-enhanced wet adhesion on insect-inspired fibrillar adhesive pads. *Nat. Commun.* **6**, 6621 (2015).
44. Y. Zheng, H. Bai, Z. Huang, X. Tian, F.-Q. Nie, Y. Zhao, J. Zhai, L. Jiang, Directional water collection on wetted spider silk. *Nature* **463**, 640–643 (2010).
45. L. Liu, X. Li, M. Nagao, A. L. Elias, R. Narain, H.-J. Chung, A pH-Indicating colorimetric tough hydrogel patch towards applications in a substrate for smart wound dressings. *Polymers* **9**, 558 (2017).
46. C. Cie, *Commission Internationale de l'Éclairage Proceedings* (Cambridge University, 1932).
47. S. L. Kolar, C.-M. Tsai, J. Torres, X. Fan, H. Li, G. Y. Liu, *Propionibacterium acnes*–induced immunopathology correlates with health and disease association. *JCI Insight* **4**, e124687 (2019).
48. E. Papakonstantinou, A. J. Aletras, E. Glass, P. Tsogas, A. Dionyssopoulos, J. Adjaye, S. Fimmel, P. Gouvousis, R. Herwig, H. Lehrach, C. C. Zouboulis, G. Karakiulakis, Matrix metalloproteinases of epithelial origin in facial sebum of patients with acne and their regulation by isotretinoin. *J. Invest. Dermatol.* **125**, 673–684 (2005).
49. R. Gunathilake, N. Y. Schurer, B. A. Shoo, A. Celli, J.-P. Hachem, D. Crumrine, G. Sirimanna, K. R. Feingold, T. M. Mauro, P. M. Elias, pH-regulated mechanisms account for pigment-type differences in epidermal barrier function. *J. Invest. Dermatol.* **129**, 1719–1729 (2009).
50. S. H. Youn, C. W. Choi, J. W. Choi, S. W. Youn, The skin surface pH and its different influence on the development of acne lesion according to gender and age. *Skin Res. Technol.* **19**, 131–136 (2013).
51. S. Baik, D. W. Kim, Y. Park, T.-J. Lee, S. H. Bhang, C. Pang, A wet-tolerant adhesive patch inspired by protuberances in suction cups of octopi. *Nature* **546**, 396–400 (2017).
52. C. T. Nguyen, S. K. Sah, C. C. Zouboulis, T.-Y. Kim, Inhibitory effects of superoxide dismutase 3 on *Propionibacterium acnes*-induced skin inflammation. *Sci. Rep.* **8**, 4024 (2018).
53. D. Pornpattananangkul, V. Fu, S. Thamphiwatana, L. Zhang, M. Chen, J. Vecchio, W. Gao, C.-M. Huang, L. Zhang, In vivo treatment of *Propionibacterium acnes* infection with liposomal lauric acids. *Adv. Healthc. Mater.* **2**, 1322–1328 (2013).
54. C. O. Chantre, P. H. Campbell, H. M. Golecki, A. T. Buganza, A. K. Capulli, L. F. Deravi, S. Dauth, S. P. Sheehy, J. A. Paten, K. Gledhill, Y. S. Doucet, H. E. Abaci, S. Ahn, B. D. Pope, J. W. Ruberti, S. P. Hoerstrup, A. M. Christiano, K. K. Parker, Production-scale fibronectin nanofibers promote wound closure and tissue repair in a dermal mouse model. *Biomaterials* **166**, 96–108 (2018).
55. J. Ye, H. Piao, J. Jiang, G. Jin, M. Zheng, J. Yang, X. Jin, T. Sun, Y. H. Choi, L. Li, G. Yan, Polydatin inhibits mast cell-mediated allergic inflammation by targeting PI3K/Akt, MAPK, NF-κB and Nrf2/HO-1 pathways. *Sci. Rep.* **7**, 11895 (2017).
56. A. M. Barbero, H. F. Frasch, Pig and guinea pig skin as surrogates for human in vitro penetration studies: A quantitative review. *Toxicol. In Vitro* **23**, 1–13 (2009).
57. E. Kroner, R. Maboudian, E. Arzt, Adhesion characteristics of PDMS surfaces during repeated pull-off force measurements. *Adv. Eng. Mater.* **12**, 398–404 (2010).
58. L. Heepe, M. Varenberg, Y. Itovich, S. N. Gorb, Suction component in adhesion of mushroom-shaped microstructure. *J. R. Soc. Interface* **8**, 585–589 (2010).

Acknowledgments: We thank W. Lee for designing the pH-sensing software. **Funding:** We gratefully acknowledge support from the National Research Foundation of Korea (NRF-2019R1C1C1008730). This work has been conducted with the support of the Korea Health Technology R&D Project (grant HP20C0078). This work was supported by the Korea Evaluation Institute of Industrial Technology (KEIT) grant funded by the Korean government (MSIT) (No. 20009125). This work was also supported by the Institute for Basic Science (IBS-R026-D1). **Author contributions:** S.B., J.L., E.J.J., S.-W.C., and C.P. conceived this project. S.B., J.L., D.W.K., and C.P. developed the experimental setup for adhesion tests and liquid collection measurements. S.B. and J.L. performed adhesion experiments. J.H.S. and H.J.L. used FEM simulation to verify the adhesion principle. S.B., J.L., and D.W.K. carried out liquid collection experiments. E.J.J. and S.-W.C. designed the animal experiments. E.J.J. and S.Y.H. performed the animal experiments and histological analyses. B.-y.P. aided in constructing the machine learning model. S.B., J.L., E.J.J., B.-y.P., S.-W.C., and C.P. analyzed all the experimental data. S.B., J.L., E.J.J., H.J.L., B.-y.P., S.-W.C., and C.P. wrote this paper, and all authors provided feedback. **Competing interests:** S.B., J.L., D.W.K., and C.P. are inventors on an adhesive architecture patent application related to this work filed by SKKU (KR patent application no. 1021873490000, filed on 30 November 2020; U.S. patent application no. 16783621, filed on 6 February 2020). The authors declare no competing interests. **Data and materials availability:** All data needed to evaluate the conclusions in the paper are present in the paper and/or the Supplementary Materials.

Submitted 4 November 2020
Accepted 30 April 2021
Published 16 June 2021
10.1126/sciadv.abf5695

Citation: S. Baik, J. Lee, E. J. Jeon, B.-y. Park, D. W. Kim, J. H. Song, H. J. Lee, S. Y. Han, S.-W. Cho, C. Pang, Diving beetle–like miniaturized plungers with reversible, rapid biofluid capturing for machine learning–based care of skin disease. *Sci. Adv.* **7**, eabf5695 (2021).